INFLUENCE OF ACTIVATION ENERGY AND STEFAN BLOWING ON MAGNETO CROSS WILLIAMSON FLUID OVER AN EXPONENTIAL STRETCHING SHEET

Sujatha VARDIREDDY [1], Sridhar WURITI [2*], Raghavendra Ganesh GANUGAPATI [3], Hymavathi TALLA [4]

[1]Research Scholar, Department of Mathematics, Koneru Lakshmaiah Educational Foundation, Vaddeswaram, Gunturu, 522302, A.P., India

[2*]Department of Mathematics, Koneru Lakshmaiah Educational Foundation, Vaddeswaram, Gunturu, 522302, A.P., India

[3]Department of Mathematics, PVP Siddhardha Institute of Technology, Kanuru,Vijayawada, A.P., India, Vijayawada, 520007,A.P., India

[4]Department of Mathematics, Adikavi Nannaya University, Rajamundry, A.P., India, 533296,A.P., India

[*] Corresponding author; E-mail: sridharwuriti@gmail.com

In this study, a two-dimensional Williamson fluid flows through a Darcy-Forchhiemer permeable medium, influenced by mixed convection, MHD, and non-linear thermal radiation over an exponential stretching sheet. The impacts of Stefan blowing, Brownian motion, and thermophoresis are being studied. This investigation looks into the impacts of joule heating and activation energy. The governing partial differential equations that are used for fluid flow modelling are transformed into a collection of non-linear ordinary differential equations by use of the required similarity transformations. The Keller Box numerical technique is applied to solve the corresponding nonlinear ordinary differential equations. The influence of numerous characteristics is investigated using graphical representations of velocity, temperature, and concentration. To validate the problem, numerical values of the Nusselt number are calculated and compared to available literature. Additionally, the skin friction coefficient are determined and tabulated numerically.

Keywords : Stefan blowing, Darcy Forchhiemer permeable medium, Activation energy, Joule heating.

1. Introduction

For the purpose of treating and stimulating reservoirs, the oil industry makes use of a number of fluids that are notably non-Newtonian. They have the ability to interact with the porous formations that they are pumped through, as well as with other fluids that are contained inside the pore structure that Pearson and Tardy [1] have described. In his research, Hoyt [2] outlined the numerous uses of non-Newtonian fluid flow. These applications include the reduction of non-Newtonian fluid friction, the reduction of oil-pipeline friction, the application of surfactants to large-scale heating and cooling systems, scale-up, and flow tracing. These uses are just a few of the many available. It is explored whether single-phase liquids, solutions, and pseudo-homogeneous mixes like slurries and emulsions can be viewed as a continuum provided, they are stable and do not contain turbulent eddies, as well as how they react to sheafing that is imposed from the outside, as described by Chabra and Richardson [3]. After conducting an investigation on the flow of non-Newtonian fluids across a porous plate, Hameed and Nadeem [4] came to the conclusion that magnetic fields offer a mechanism that can regulate the expansion of boundary layers. In his research article, Mustafa [5] investigated the fluid flow upon a stretching rotating disc and came to the conclusion that raising the rotation parameter is associated with a significant rise in the near disc velocities. The magnetic field effect on fluid flows was examined by Kabeel *et al.* [6], and it has applications in a variety of fields of medicine and engineering, including MHD power generators, the cooling of gearbox lines, and boundary layer control in aerodynamics.

Through the use of nonlinear radiation modelling, it is possible to achieve optimal thermal efficiency and temperature distribution. In the process of designing components that are able to function at high temperatures, radiative heat transfer analysis is helpful. Khan and others [7]. Nanofluid flow with non-linear thermal radiation influence was analyzed, and it was found that increased radiation parameter values led to an increase in both temperature and concentration. According to Hosseinzadeh and colleagues' study on Maxwell nanofluid flow with non-linear thermal radiation influence [8], the temperature profile is directly related to the temperature ratio parameter and the radiation. Khan and Hamid [9] studied the effect of nonlinear radiation and heat sources on Williamson fluid using the RK Fehlberg integration scheme. A higher Biot number, temperature ratio factors, and thermal radiation all worked together to speed up the heat transfer rate.

When mass flow influences heat and mass transfer processes across surfaces, more specifically when phase transitions take place, a phenomenon known as the Stefan-blowing effect takes place. In order to ensure precise thermal management in engineering systems such as heat exchangers, combustors, or spaceships, it is essential to take into consideration the Stefan blowing effect. Mabood *et al.* [10] conducted a study to examine how Stefan blowing affects the flow of Maxwell nanofluid over a rotating disc. They found that the Sherwood number falls as the thermophoretic parameter values increase. In their explanation of the effect of Stefan blowing on nanofluid flow over stretching sheet, Naveen Kumar and colleagues [11] discovered that the maximum heat transfer occurred where the injection of the Stefan blowing effect over a stretching sheet. In their study on the influence of Stefan blowing on nanofluid flow under Thompson troian slip conditions, Sudip dey and colleagues [12] found that the velocity of the fluid increased when the velocity slip parameter values were increased. After conducting an analysis of the stagnation point flow of nanofluid over an exponentially stretched sheet, Bachok *et al.* [13] found that water-based nanofluid results the enhancement in the skin friction coefficient as well as the heat transfer coefficient. In the study conducted by Mustafa and colleagues [14], Maxwell fluid flow was investigated over an exponential stretching sheet. The researchers found that as the convective heating parameter was increased, the temperature profiles increased while the concentration profiles decreased. It is possible to transform electrical energy into heat energy through the process of joule heating when an electric current is sent through a material that is resistant. There are a number of uses for it in the medical field, the food processing sectors, and the industrial operations that involve thermal actuators. The influence of house heating on Williamson fluid flow was investigated by Hayat *et al.* [15], who found that an increase in temperature was recorded for progressive measurements of Eckert number. In their study, Ramesh *et al.* [16] investigated the effects of MHD and Joule heating on Casson fluid, together with marginal slip influences. They found that temperature increased with radiation, thermal slip, and Casson fluid characteristics. Ali *et al.* [17] observed the flow of Williamson nanofluids when Joule heating was applied. They discovered that the flow of the fluid decreased when the magnetic force and Darcy laws were applied to the fluid. Rao and Paramananda [18] discovered that the speed of the Williamson nanofluid reduced as the Williamson parameters increased in their study of the flow of Williamson nanofluid across a permeable, movable cylinder. The flow of Williamson nanofluid upon a stretched cylinder was investigated by researchers Zegeye *et al.* [19]. As the number of observations of the Weissenberg parameter rises, the skin friction also increases. The activation energy of a chemical reaction or a physical process is the minimal amount of energy that is necessary to commence the reaction or process. It is the barrier that molecules need to overcome in order to change into a product state. There is a correlation between activation energy and the thickness of reactive boundary layers in fluid systems. Ijaz and Ayub [20] studied how activation energy affects the flow of Walter-B fluid. They discovered that when the activation energy is larger, the concentration profiles are significantly improved. Sherwood number drops with larger observations of activation energy parameter values, according to the findings of Salahuddin *et al.* [21], who investigated Carreu fluid flow over stretchy paraboloid surface with activation energy influence. In their study of MHD cross nanofluid with activation energy impact across vertical stretching sheet, The concentration of the chemical reaction parameter decreases with increasing parameter values, whereas it increases in the case of the activation parameter, according to Srinivas Reddy and Ali [22]. Considering the impacts of Stefan blowing, heat source, permeability, non-linear radiation, and chemical reaction, Saleem and Hussain [23] investigated the Williamson nanofluid flow upon an exponentially stretched surface. According to their findings, temperature profiles for the heat source's Eckert number increased. The main focus of this study is on the effects of non-linear radiation, Joule heating, and activation energy with Stefan blowing on Williamson nanofluid flow across Darcy Forchheimer permeable medium.

2. Formulation of the problem

This study aims to examine a two-dimensional Williamson fluid in motion through an exponential stretching sheet and a Darcy-Forchhiemer permeable medium. In Stefan blowing situation

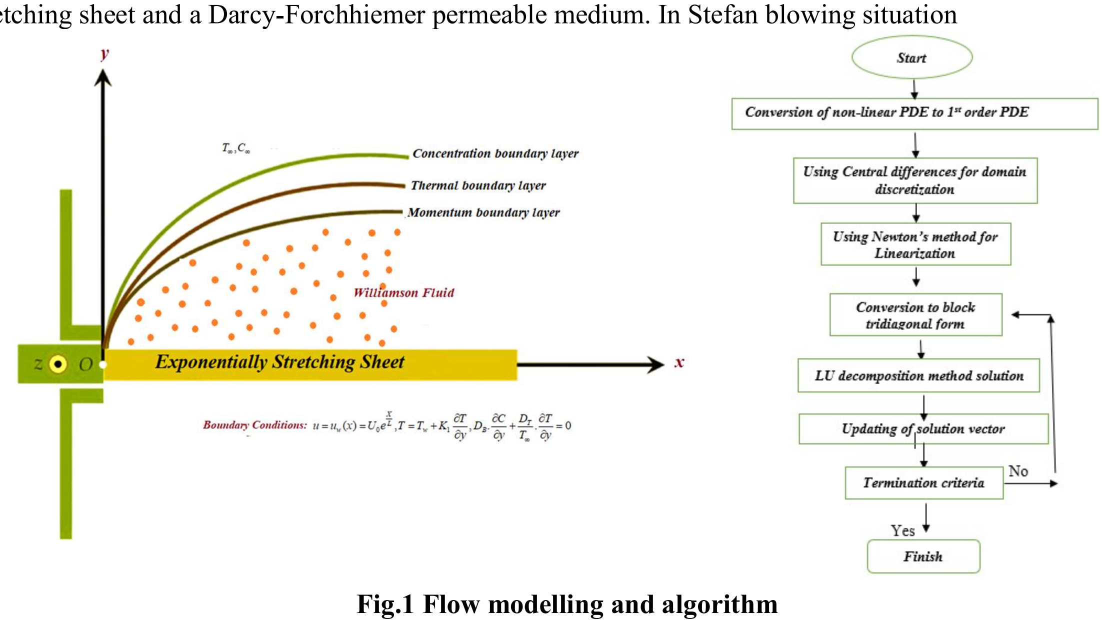

Fig.1 Flow modelling and algorithm

involving injection and suction, flow can be seen. This study includes the following aspects: activation energy, joule heating, and non-linear thermal radiation. The following components make up the model-corresponding partial differential equations, taking into account the assumptions [23].

$$\frac{\partial u}{\partial x}+\frac{\partial u}{\partial y}=0 \tag{1}$$

$$u\frac{\partial u}{\partial x}+v\frac{\partial u}{\partial y}=\upsilon\frac{\partial^2 u}{\partial y^2}+\sqrt{2}\upsilon\Gamma\frac{\partial^2 u}{\partial y^2}\frac{\partial u}{\partial y}-\left(\frac{\sigma B_0^2}{\rho}+\frac{\upsilon}{k*}\right)u-\frac{C_b}{\sqrt{k*}}u^2+g\beta^*\left(T-T_\infty\right) \tag{2}$$

$$u\frac{\partial T}{\partial x}+v\frac{\partial T}{\partial y}=\alpha\frac{\partial^2 T}{\partial y^2}+\frac{\left(\rho c_p\right)_p}{\left(\rho c_p\right)_f}\left[D_B\frac{\partial C}{\partial y}\frac{\partial T}{\partial y}+\frac{D_T}{T_\infty}\left(\frac{\partial T}{\partial y}\right)^2\right]-\frac{1}{\left(\rho c_p\right)_f}\frac{\partial q_r}{\partial y}+\frac{\sigma B_0^2}{\left(\rho c_p\right)_f}u^2 \tag{3}$$

$$u\frac{\partial C}{\partial x}+v\frac{\partial C}{\partial y}=D_B\frac{\partial^2 C}{\partial y^2}+\frac{D_T}{T_\infty}\frac{\partial^2 T}{\partial y^2}-k_r^2(C-C_\infty)\left(\frac{T}{T_\infty}\right)^m\exp\left(-\frac{Ea}{k_1 T}\right) \tag{4}$$

The non-linear thermal radiation term is given by $q_r=-\frac{4}{3}\frac{\sigma}{k^*}\frac{\partial T^4}{\partial y}=-\frac{16\sigma}{3k^*}T^3\frac{\partial T}{\partial y}$

then, the equation (3) takes the form

$$\begin{aligned}u\frac{\partial T}{\partial x}+v\frac{\partial T}{\partial y}&=\alpha\frac{\partial^2 T}{\partial y^2}+\frac{\left(\rho c_p\right)_p}{\left(\rho c_p\right)_f}\left[D_B\frac{\partial C}{\partial y}\frac{\partial T}{\partial y}+\frac{D_T}{T_\infty}\left(\frac{\partial T}{\partial y}\right)^2\right]\\&+\frac{16\sigma}{3k^*\left(\rho c_p\right)_f}\left[3T^2\left(\frac{\partial T}{\partial y}\right)^2+T^3\frac{\partial^2 T}{\partial y^2}\right]+\frac{\sigma B_0^2}{\left(\rho c_p\right)_f}u^2\end{aligned} \tag{5}$$

Corresponding bc's are

$$u=u_w(x)=U_0e^{\frac{X}{L}},v=-\frac{D_B}{1-C_w}\frac{\partial C}{\partial y},T=T_w+K_1\frac{\partial T}{\partial y},D_B.\frac{\partial C}{\partial y}+\frac{D_T}{T_\infty}.\frac{\partial T}{\partial y}=0\,at\,y=0$$

$$u\to 0,T\to T_\infty,C\to C_\infty \text{ as } y\to\infty$$

Using the similarity transformations

$$\begin{aligned}&\eta=\sqrt{\frac{U_0}{2\upsilon L}}e^{\frac{X}{2L}}y,u=U_0e^{\frac{X}{L}}f'(\eta),v=-\sqrt{\frac{U_0\upsilon}{2\upsilon L}}e^{\frac{X}{2L}}f(\eta)-\frac{U_0}{2L}e^{\frac{X}{L}}yf'(\eta)\\&T=T_\infty+T_0e^{\frac{X}{2L}}\theta(\eta),C=C_\infty+C_0e^{\frac{X}{2L}}\phi(\eta),T=T_\infty\left[1+\left(\theta_w-1\right)\theta(\eta)\right]\\&\theta_w=\frac{T_w}{T_\infty}\end{aligned} \tag{6}$$

Equations (2, 4, 5) can be converted to

$$f'''(\eta)+\lambda f''(\eta)f'''(\eta)-(M^2+kp)f'(\eta)+f(\eta)f''(\eta)-2f'^2(\eta)+Rie^{\frac{-3}{2}X_\lambda}\theta(\eta)=0 \tag{7}$$

$$\begin{aligned}&\theta''(\eta)-\Pr f'(\eta)\theta(\eta)+\Pr f(\eta)\theta'(\eta)+\Pr Jf'^2(\eta)\\&+\Pr Nb\theta'(\eta)\phi'(\eta)+\Pr Nt\theta'^2+\Pr R_\lambda\left(1+\left(\theta_w-1\right)\theta(\eta)\right)^3\\&+3\Pr R_\lambda(\theta_w-1)\left(1+\left(\theta_w-1\right)\theta(\eta)\right)^2\theta''=0\end{aligned} \tag{8}$$

$$\phi''(\eta)+\frac{Nt}{Nb}\theta''(\eta)+Scf(\eta)\phi'(\eta)-Scf'(\eta)\phi(\eta)-Sc\sigma\phi(\eta)\left(1+\delta\theta(\eta)\right)^m\exp\left(-\frac{E_0}{1+\delta\theta(\eta)}\right)=0 \tag{9}$$

Also, boundary conditions are converted to

$$f(0)=\frac{S}{Sc}\phi'(0), f'(0)=1, \theta(0)=1+\delta_T\theta'(0), Nb\phi'(0)+Nt\theta'(0)=0$$
$$f'\to 0, \theta\to 0, \phi\to 0 \quad (10)$$
$$as\eta\to\infty$$

2. Solution methodology

The Keller box method is a numerical methodology used to solve equations (7-9) to first-order ordinary differential equations. Newton's method is used to linearize the following equations using finite differences, and they are subsequently expressed in matrix form. The tri-diagonal elimination method or the LU decomposition method is then used to solve the equations.

Introducing $\frac{\partial f}{\partial\eta}=p, \frac{\partial p}{\partial\eta}=q, \frac{\partial g}{\partial\eta}=t, \frac{\partial s}{\partial\eta}=n \, where\, g=\theta, s=\phi$, equations 7-9 becomes

$$q'+\lambda qq'-(M^2+kp)p+fq-2p^2+Rie^{\frac{-3}{2}X_\lambda}g=0 \quad (11)$$

$$t'-\Pr pg+\Pr ft+\Pr Jp^2+\Pr Nbtn+\Pr Ntt^2+$$
$$\Pr R_\lambda\left(1+\left(\theta_w-1\right)g\right)^3+3\Pr R_\lambda(\theta_w-1)\left(1+\left(\theta_w-1\right)g\right)^2t'=0 \quad (12)$$

$$n'+\frac{Nt}{Nb}t'+Scfn-Scps-Sc\sigma s\left(1+\delta g\right)^m\exp\left(-\frac{E_0}{1+\delta g}\right)=0 \quad (13)$$

applying, finite differences for the equations $\frac{\partial f}{\partial\eta}=p, \frac{\partial p}{\partial\eta}=q, \frac{\partial g}{\partial\eta}=t, \frac{\partial s}{\partial\eta}=n$ and equations (11)-(13) and using Newton's method to linearize the equations we get the system of equations as follows

$$\delta f_j-\delta f_{j-1}=\left(r_1\right)_j+0.5h_j(\delta p_j+\delta p_{j-1})$$
$$\delta p_j-\delta p_{j-1}=\left(r_2\right)_j+0.5h_j(\delta q_j+\delta q_{j-1})$$
$$\delta g_j-\delta g_{j-1}=\left(r_3\right)_j+0.5h_j(\delta t_j+\delta t_{j-1})$$
$$\delta s_j-\delta s_{j-1}=\left(r_4\right)_j+0.5h_j(\delta n_j+\delta n_{j-1})$$
$$\left(r_5\right)_j=\left(a_1\right)_j\delta q_j+\left(a_2\right)_j\delta q_{j-1}+\left(a_3\right)_j\delta p_j+\left(a_4\right)_j\delta p_{j-1}+\left(a_5\right)_j\delta f_j+\left(a_6\right)_j\delta f_{j-1}+\left(a_7\right)_j\delta g_j+\left(a_8\right)_j\delta g_{j-1}$$
$$\left(r_6\right)_j=\left(b_1\right)_j\delta t_j+\left(b_2\right)_j\delta t_{j-1}+\left(b_3\right)_j\delta f_j+\left(b_4\right)_j\delta f_{j-1}+\left(b_5\right)_j\delta g_j$$
$$+\left(b_6\right)_j\delta g_{j-1}+\left(b_7\right)_j\delta p_j+\left(b_8\right)_j\delta p_{j-1}+\left(b_9\right)_j\delta n_j+\left(b_{10}\right)_j\delta n_{j-1}$$
$$\left(r_7\right)_j=\left(c_1\right)_j\delta n_j+\left(c_2\right)_j\delta n_{j-1}+\left(c_3\right)_j\delta t_j+\left(c_4\right)_j\delta t_{j-1}+\left(c_5\right)_j\delta f_j$$
$$+\left(c_6\right)_j\delta f_{j-1}+\left(c_7\right)_j\delta s_j+\left(c_8\right)_j\delta s_{j-1}+\left(c_9\right)_j\delta g_j+\left(c_{10}\right)_j\delta g_{j-1}+\left(c_{11}\right)_j\delta p_j+\left(c_{12}\right)_j\delta p_{j-1}$$

The resulting system of equations can be arranged into tri-diagonal system as

$$\left[A_1\right]\left[\delta_1\right]+\left[C_1\right]\left[\delta_2\right]=\left[r_1\right]$$
$$\left[B_2\right]\left[\delta_1\right]+\left[A_2\right]\left[\delta_2\right]+\left[C_2\right]\left[\delta_3\right]=\left[r_2\right]$$
$$\cdots\cdots\left[B_{j-1}\right]\left[\delta_1\right]+\left[A_{j-1}\right]\left[\delta_2\right]+\left[C_{j-1}\right]\left[\delta_3\right]=\left[r_{j-1}\right]$$
$$\left[B_j\right]\left[\delta_{j-1}\right]+\left[A_j\right]\left[\delta_j\right]=\left[r_j\right] \qquad \text{for j=1,2,....}$$

where,

$$
(A_1)=\begin{bmatrix}
0 & 0 & 0 & 1 & 0 & 0 & 0\\
-\frac{h_j}{2} & 0 & 0 & 0 & -\frac{h_j}{2} & 0 & 0\\
0 & -\frac{h_j}{2} & 0 & 0 & 0 & -\frac{h_j}{2} & 0\\
0 & 0 & -1 & 0 & 0 & 0 & -\frac{h_j}{2}\\
(a_2)_1 & 0 & 0 & (a_5)_1 & (a_1)_1 & 0 & 0\\
0 & (b_2)_1 & 0 & (b_5)_1 & 0 & (b_1)_1 & (b_3)_1\\
0 & (c_4)_1 & (c_8)_1 & (c_5)_1 & 0 & (c_3)_1 & (c_1)_1
\end{bmatrix}
\quad
(A_j)=\begin{bmatrix}
-\frac{h_j}{2} & 0 & 0 & 1 & 0 & 0 & 0\\
-1 & 0 & 0 & 0 & -\frac{h_j}{2} & 0 & 0\\
0 & -1 & 0 & 0 & 0 & -\frac{h_j}{2} & 0\\
0 & 0 & -1 & 0 & 0 & 0 & -\frac{h_j}{2}\\
(a_4)_j & (a_8)_j & 0 & (a_5)_j & (a_1)_j & 0 & 0\\
(b_{10})_j & (b_8)_j & 0 & (b_5)_j & (b_9)_j & (b_1)_j & (b_3)_j\\
(c_{10})_j & 0 & (c_8)_j & (c_5)_j & 0 & (c_3)_j & (c_1)_j
\end{bmatrix}
$$

$$
(B_j)=\begin{bmatrix}
0 & 0 & 0 & -1 & 0 & 0 & 0\\
0 & 0 & 0 & 0 & -\frac{h_j}{2} & 0 & 0\\
0 & 0 & 0 & 0 & 0 & -\frac{h_j}{2} & 0\\
0 & 0 & 0 & 0 & 0 & 0 & -\frac{h_j}{2}\\
0 & 0 & 0 & (a_6)_j & (a_2)_j & 0 & 0\\
0 & 0 & 0 & (b_6)_j & 0 & (b_2)_j & (b_4)_j\\
0 & 0 & 0 & (c_6)_j & 0 & (c_4)_j & (c_2)_j
\end{bmatrix}
\quad
(C_j)=\begin{bmatrix}
-\frac{h_j}{2} & 0 & 0 & 0 & 0 & 0 & 0\\
1 & 0 & 0 & 0 & 0 & 0 & 0\\
0 & 1 & 0 & 0 & 0 & 0 & 0\\
0 & 0 & 1 & 0 & 0 & 0 & 0\\
(a_3)_j & (a_7)_j & 0 & 0 & 0 & 0 & 0\\
(b_9)_j & (b_7)_j & 0 & 0 & 0 & 0 & 0\\
(c_{11})_j & (c_9)_j & (c_7)_j & 0 & 0 & 0 & 0
\end{bmatrix}
$$

We solved the resulting system of equations using LU decomposition method. The computations are performed until the convergence criteria is reached where ε=0.00001.

Skin friction, Nusselt number and, Sherwood numbers are to be calculated using the

$$\sqrt{2\,\mathrm{Re}}C_f=\left[f''+\lambda\left(f''\right)^2\right]_{\eta=0},\ \frac{Nu_x}{\sqrt{\mathrm{Re}}}=-\left[\left(1+R_\lambda\theta_w^3\right)\theta'\right]_{\eta=0},\ \frac{Sh_x}{\sqrt{\mathrm{Re}}}=-\phi'(0)$$

4. Results and Discussion

To study the influence of several parameters on the fluid flow graphs are plotted to analyse velocity, temperature, and concentration characteristics using MATLAB [24].

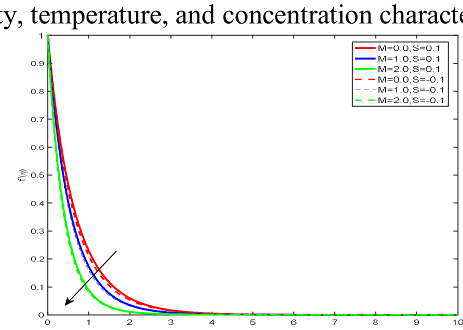

Fig.2 Variation of f' for Magnetic Parameter M

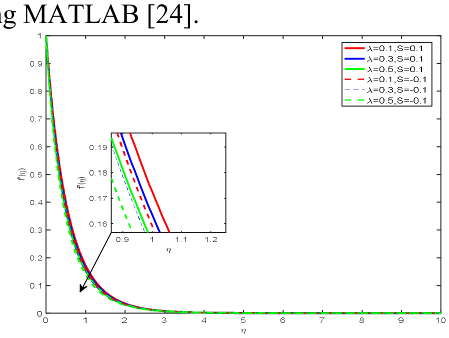

Fig.3 Variation of f' for λ

Illustrations of M's velocity profiles can be found in Figure 2. Because of the increased measurements of magnetic properties, an opposing force is formed, which results in a decrease in fluid flow in both instances of Stefan blowing (S>0 and S<0). The viscosity of the material reduces as and when the shear rate increases for increasing values of. Thus, in order to achieve higher values of the Williamson fluid parameter. Figure 3 illustrates the reduction in velocity profile that occurs in both instances of Stefan blowing (S>0 and S<0). Increasing the Forchhiemer parameter results reveal that the generation of a frictional force inside the fluid, which leads to a decrement in the velocity of the fluid flow in both instances of Stefan blowing (S>0, S<0), as seen in Figure 4. Figure 5 illustrates the velocity patterns of the porous parameter Kp for both instances of Stefan blowing (S>0 and S<0).

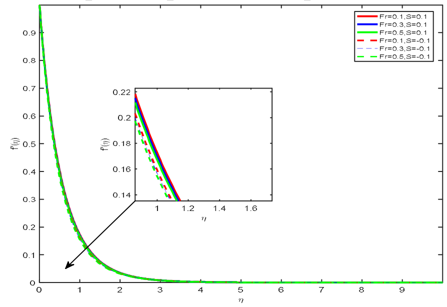

Fig.4 Variation of f' for Fr

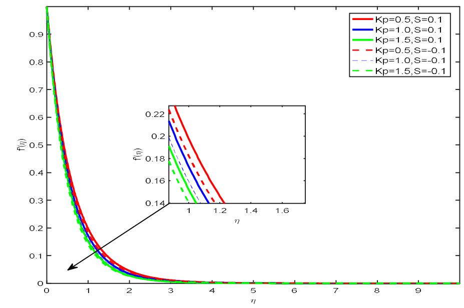

Fig. 5 Variation of f' for Kp

Increasing the resistive force of the porous parameter results reveal that decrease in the fluid flow velocity. A representation of the velocity profiles of Ri is shown in Figure 6 for both instances of Stefan blowing (S>0 and S<0). A decrease in fluid flow is the result of an increase in the natural convection coefficient, which is caused by an increase in the Richardson parameter. Figure 7 illustrates the velocity profiles of both the Stefan blowing scenarios (S>0 and S<0) in the context of the phenomenon. A decrease in fluid flow is noted when there is an increase in the number of observations.

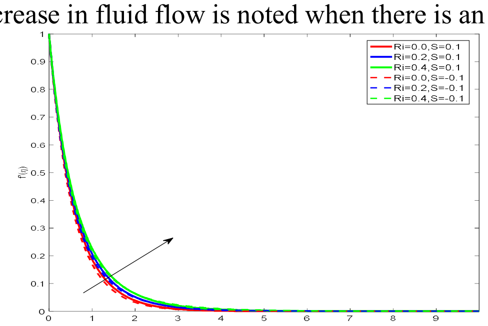

Fig.6 Variation of f' for Ri

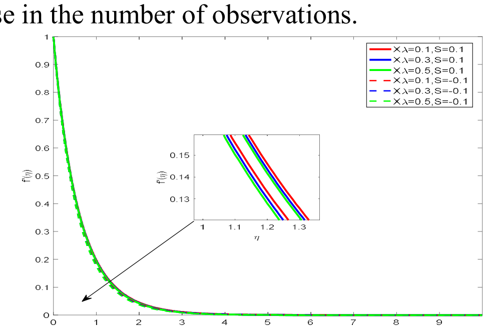

Fig.7 Variation of f' for X_λ

For both cases of Stefan blowing (S>0 and S<0), figure 8 shows the temperature profiles of M. The fluid flow temperature is increased as a consequence of an increase in the thermal boundary layer thickness due to improved measurements of magnetic parameters. The temperature patterns of the Williamson fluid parameter are displayed visually in Figure 9. By observing the progression of the Williamson fluid parameter, it is found that there is an improvement in the elasticity stress parameter, which results in a rise in temperature for both instances of Stefan blowing (S>0, St<0). Figure 10 presents comprehensive temperature profiles of the Forchheimer parameter. An elevation in the Forchheimer parameter values results in an augmentation of the inertial effect on fluid flow, thereby generating resistance in fluid movement. As a result, temperature distribution increases in both cases of Stefan blowing (S>0 and S<0). As the Porosity parameter increases, there is a noticeable enhancement in temperature profiles being observed for both instances of Stefan blowing (S>0 and S<0) in figure 11. The temperature outlines of the Richardson parameter are displayed in Figure 12. This parameter causes an increase in the heat transfer rate, which results in a declination in the temperature profiles for both situations of Stefan blowing (S>0, S<0). Detailed temperature profiles of are depicted in Figure 13. Increasing the thickness size of the thermal boundary layer leads to an enhancement in the temperature of the fluid flow for both cases of Stefan blowing (S>0.S<0).

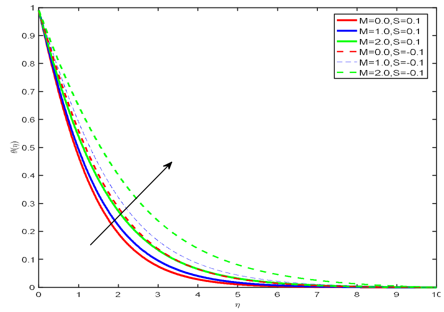

Fig.8 Variation of $\theta(\eta)$ for M

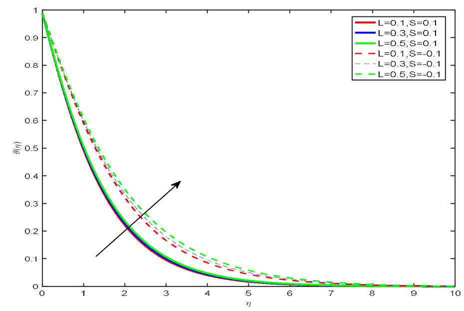

Fig.9 Variation of $\theta(\eta)$ for L

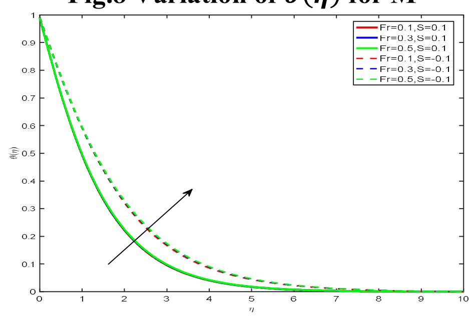

Fig.10 Variation of $\theta(\eta)$ for Fr

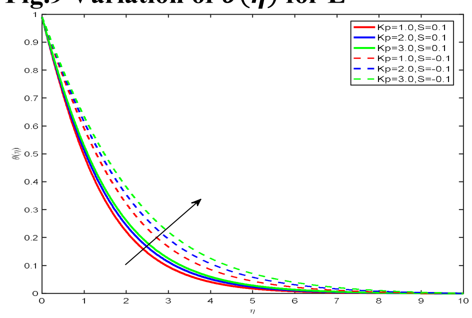

Fig.11 Variation of $\theta(\eta)$ for Kp

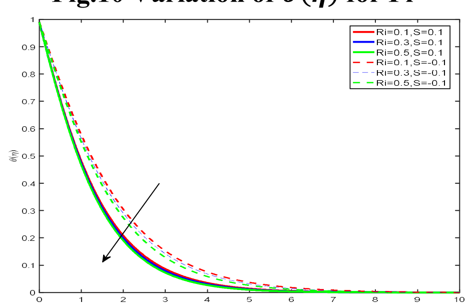

Fig.12 Variation of $\theta(\eta)$ for Ri

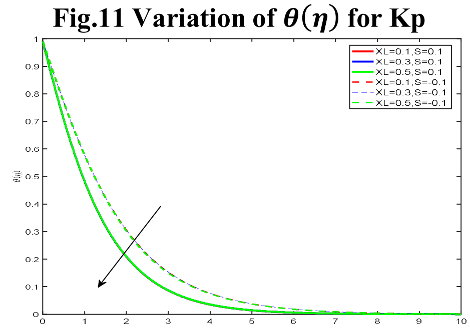

Fig.13 Variation of $\theta(\eta)$ for X_{λ}

This is the case for greater observations of the thermal boundary layer. As the Prandtl number increases, the thermal conductivity of the fluid drops, which results in a fall in temperature profiles.

This phenomenon is observed in both cases of Stefan blowing (S>0, S<0), as visually represented in figure 14. Figure 15 shows the Joule heating parameter's temperature curves. The temperature of the conductor rises with higher values of the joule heating parameter, leading to an improvement in the temperature profiles for both the Stefan blowing instances (S>0, S<0). Pictures 16, 17 show the radiation parameter and temperature profiles. The temperature of the fluid rises in both the Stefan blowing instances (S>0, S<0) when the radiation parameter's elevated values cause an increase in the heat dispersion. Fig. 18, 19 show the radiation parameter and the temperature ratio parameter's concentration patterns. In both cases of Stefan blowing (S>0, S<0), there is a decrease in concentration profiles due to an increase in the boundary layer thickness of the concentration, which allows for better observations of the radiation parameter, temperature ratio parameter, and concentration. Representation of concentration profiles of the Schmidt number is shown in Figure 20. For the increased observations of Schmidt number mass transfer enhancement is observed. So, the concentration of the fluid increases in both cases of Stefan blowing (S>0, S<0). Figure 21 represents concentration profiles of Brownian motion parameter. Increasing Brownian motion parameter, the concentration profile increases in both cases of Stefan blowing(S>0, S<0).

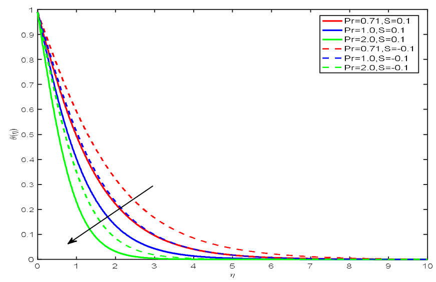

Fig.14 Variation of $\theta(\eta)$ for Pr

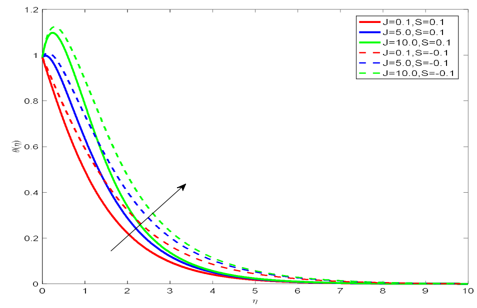

Fig.15 Variation of $\theta(\eta)$ for J

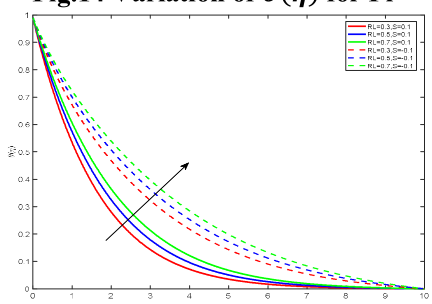

Fig.16 Variation of $\theta(\eta)$ for R_{λ}

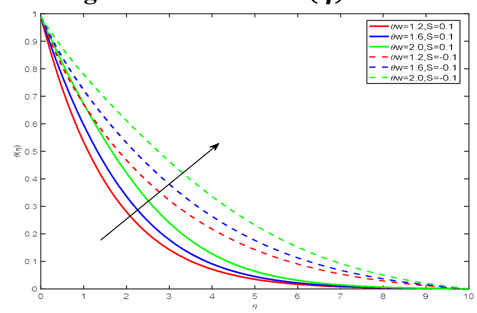

Fig.17 Variation of $\theta(\eta)$ for θ_w

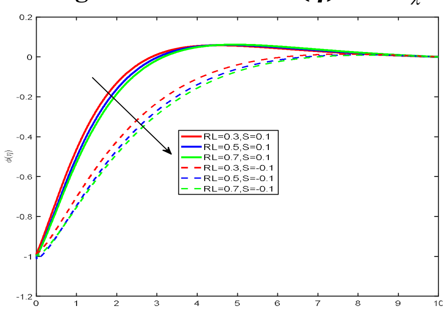

Fig.18 Variation of $\phi(\eta)$ for R_{λ}

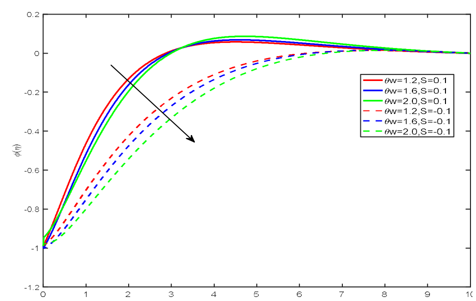

Fig.19 Variation of $\phi(\eta)$ for θ_w

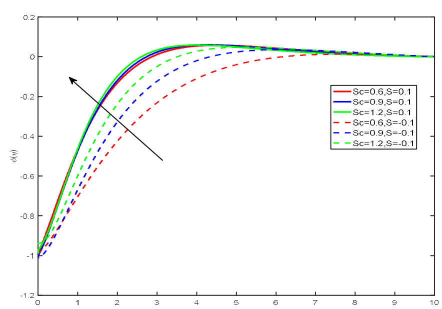

Fig.20 Variation of $\phi(\eta)$ for Sc

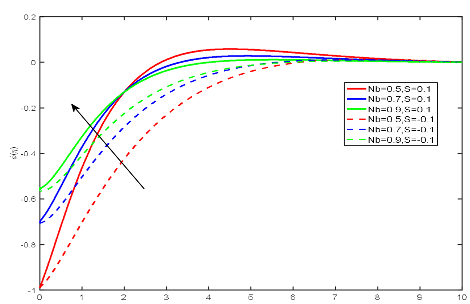

Fig.21 Variation of $\phi(\eta)$ for Nb

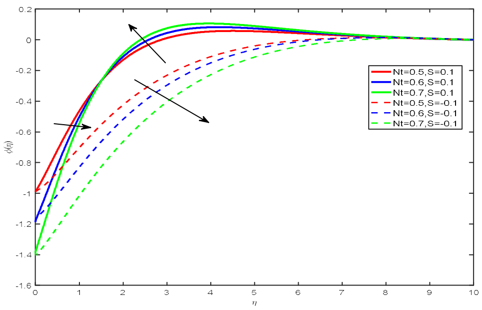

Fig.22 Variation of $\phi(\eta)$ for Nt

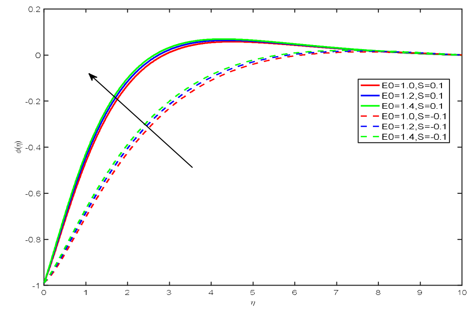

Fig.23 Variation of $\phi(\eta)$ for E_0

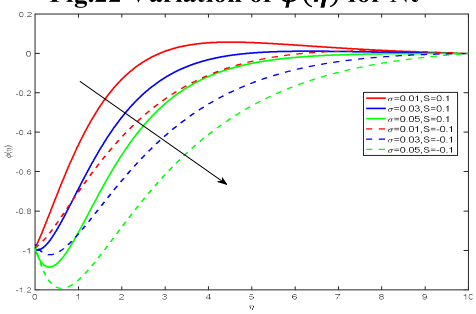

Fig.24 Variation of $\phi(\eta)$ for σ

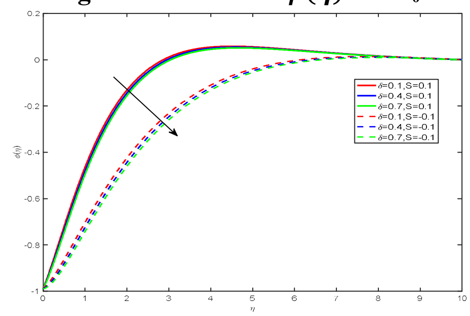

Fig.25 Variation of $\phi(\eta)$ for δ

Thermophoresis parameter concentration curves are shown in Figure 22. In the case of Stefan blowing (S<0), the parameter concentration drops for increasing values of thermophoresis, initially declines for, and then increases afterwards. Figure 23 depicts Concentration profiles of E_0, For the enhanced values of E_0 nanoparticle concentration is enhanced by rising E_0 values. Low temperature and high activation causing an increase concentration by slowing down the order of reaction, which in turn causes a rise in concentration profiles. Figure 24 displays Concentration profiles of the reaction rate parameter. For enhanced values of the reaction rate parameter, the concentration profiles are decreasing. For higher values of concentration profile declines which is depicted in Figure 25. Skin friction values are calculated for various values of Williamson fluid parameter, Stefan blowing parameter and Magnetic parameter and tabulated in table 2. Also, Nusselt number is calculated for distinct values of Williamson fluid parameter at two different cases of Stefan blowing parameter and compared with existing literature and Results are good and consistent with the previous literature mentioned in table1.

Table1. Comparison of $-\theta'(0)$ values for various values of λ

λ	S=0.1		S=-0.1	
	Saleem and Hussain [23]	Current results	Saleem and Hussain [23]	Current results
0.1	0.566485525	0.5664223340	0.612563075	0.6126574590
0.2	0.560865769	0.5608358470	0.606017281	0.6089577250
0.3	0.554427672	0.5536728830	0.598360110	0.5989374340

Table2. Skin friction coefficient values for various values of λ, S, M

λ	S	M	$-\sqrt{2\,\mathrm{Re}}C_f$
0.1	0.2	2.0	2.09760
0.2			1.87513
0.3			1.59887
	-0.1		1.63757
	0.0		1.62594
	0.1		1.61298
		0.0	1.07366
		1.0	1.29025
		2.0	1.61298

5. Conclusions

In the present paper MHD Williamson fluid flow is examined through Darcy Forchhiemer permeable medium with the influence of Stefan blowing, Joule heating, non-linear thermal radiation, and Activation energy. The corresponding equations of the model are solved using the Keller Box numerical scheme and graphs are plotted the following conclusions are obtained.

1. Velocity profile declines for Magnetic, Williamson, X_λ, Porous and Forchhiemer parameters and enhances for Richardson parameter.
2. Temperature profiles enhanced for Magnetic, Williamson, Forchhiemer, Joule heating, porous, thermal radiation, and temperature ratio parameters and the reverse trend is observed in the case of X_λ, Prandtl number.
3. Concentration profile increases in the case of Schmidt number and activation energy parameters and the reverse trend is witnessed for radiation, temperature ratio, reaction rate and temperature difference parameters.
4. Skin friction value decreases for the progressive values of the Williamson parameter, the magnetic parameter, and the Stefan blowing parameters.

Nomenclature:

u,v	Velocity components ($m.s^{-1}$)	ρ	Density ($kg.m^{-3}$)
υ	Kinematic viscosity (m^2s^{-1})	k_1	Boltzman constant
λ	Williamson fluid parameter	k^*	Permeability of the Porous medium(m^2)
T	Fluid temperature (^0C)	C_p	Specific heat at constant
T_∞	Ambient fluid temperature	k_r	Reaction rate ($mol\cdot L^{-1}\cdot s^{-1}$)
D	Diffusion coefficient (m^2s^{-1})	C_0	Fluid concentration ($kg.m^{-3}$)
μ	Dynamic viscosity ($N.s.m^{-2}$)	C_∞	Ambient fluid concentration (kg/m^3)
k	Thermal conductivity ($W.m^{-1}K^{-1}$)	Q	Heat absorption/generation (kelvin)
Nt	Thermophoresis parameter	Ea	Activation energy(joules)
Nb	Brownian motion parameter	Sc	Schmidt number
M	Magnetic Parameter	R	Radiation parameter
σ	Electrical conductivity($ohm^{-1}m^{-1}$)	q_r	Radiative heat flux ($W.m^{-2}$)
Pr	Prandtl number	J	Joule heating parameter

References

[1] Pearson, J.R.A., *et al.,* Models for Flow of Non-Newtonian and Complex Fluids through Porous Media, *Journal of Non-Newtonian Fluid Mechanics*,102 (2002),pp.447–73. https://doi.org/10.1016/s0377-0257(01)00191-4.

[2] Hoyt, J.W.,Some Applications of Non-Newtonian Fluid Flow,*Advances in the Flow and Rheology of Non-Newtonian Fluids*,8 (1999), pp.797–826. https://doi.org/10.1016/s0169-3107(99)80008-2.

[3] Chhabra, R.P., *et al.*, Non-Newtonian Fluid Behaviour, *Non-Newtonian Flow in the Process Industries*, 1999,pp. 1–36. https://doi.org/10.1016/b978-075063770-1/50002-6.

[4] Hameed, M., and S. Nadeem, Unsteady MHD Flow of a Non-Newtonian Fluid on a Porous Plate.” Journal of Mathematical Analysis and Applications 325, (2007), pp.724–33. https://doi.org/10.1016/j.jmaa.2006.02.002.

[5] Turkyilmazoglu, Mustafa, MHD Fluid Flow and Heat Transfer Due to a Stretching Rotating Disk, *International Journal of Thermal Sciences*, 51, (2012),pp.195–201. https://doi.org/10.1016/j.ijthermalsci.2011.08.016.

[6] Kabeel AE *et al.,* A review of magnetic field effects on flow and heat transfer in liquids: Present status and future potential for studies and applications, *Renewable and Sustainable Energy Reviews*,45,(2015),pp.830–837. http://dx.doi.org/10.1016/j.rser.2015.02.029

[7] Khan, Umar *et al.,* Nonlinear Radiation Effects on Flow of Nanofluid over a Porous Wedge in the Presence of Magnetic Field, *International Journal of Numerical Methods for Heat & Fluid Flow* 27, (2017),pp.48–63. https://doi.org/10.1108/hff-10-2015-0433.

[8] Hosseinzadeh, Kh. *et al.,*Nonlinear Thermal Radiation and Chemical Reaction Effects on Maxwell Fluid Flow with Convectively Heated Plate in a Porous Medium,*Heat Transfer-Asian Research* 48,(2018), pp.744–59. https://doi.org/10.1002/htj.21404.

[9] Khan, Masood and Aamir Hamid, Influence of Non-Linear Thermal Radiation on 2D Unsteady Flow of a Williamson Fluid with Heat Source/Sink, *Results in Physics* 7 (2017), pp.3968–75. https://doi.org/10.1016/j.rinp.2017.10.014.

[10] Mabood, F., A.*et al.*, Impacts of Stefan Blowing and Mass Convention on Flow of Maxwell Nanofluid of Variable Thermal Conductivity about a Rotating Disk,*Chinese Journal of Physics* 71 (2021), pp.260–72. https://doi.org/10.1016/j.cjph.2021.03.003.

[11] Naveen Kumar, R. *et al.,* Stefan Blowing Effect on Nanofluid Flow over a Stretching Sheet in the Presence of a Magnetic Dipole, *Micro and Nanofluid Convection with Magnetic Field Effects for Heat and Mass Transfer Applications Using MATLAB*, 2022, 91–111. https://doi.org/10.1016/b978-0-12-823140-1.00005-1.

[12] Dey, Sudip, *et al.,*Effects of Stefan Blowing on Mixed Convection Heat Transfer in a Nanofluid Flow with Thompson and Troian Slip, *Numerical Heat Transfer, Part A: Applications*,(2023),pp. 1–20. https://doi.org/10.1080/10407782.2023.2261626.

[13] Bachok, Norfifah *et al.*,.Boundary Layer Stagnation-Point Flow and Heat Transfer over an Exponentially Stretching/Shrinking Sheet in a Nanofluid, *International Journal of Heat and Mass Transfer*, 55,(2012),pp.8122–28. https://doi.org/10.1016/j.ijheatmasstransfer.2012.08.051.

[14] Mustafa, M., *et al.,*Simulations for Maxwell Fluid Flow Past a Convectively Heated Exponentially Stretching Sheet with Nanoparticles, *AIP Advances*, 5, (2015) 037133. https://doi.org/10.1063/1.4916364.

[15] Hayat, T. *et al.,* Newtonian and Joule Heating Effects in Two-Dimensional Flow of Williamson Fluid, *Journal of Applied FluidMechanics* 9,(2016),pp.196975. https://doi.org/10.18869/acadpub.jafm.68.235.24646.

[16] Ramesh, K., *et al.,*Simultaneous Effects of MHD and Joule Heating on the Fundamental Flows of a Casson Liquid with Slip Boundaries, *Propulsion and Power Research*,10,(2021),pp.118-129. https://doi.org/10.1016/j.jppr.2021.05.002.

[17] Ali, Aatif *et al.,* MHD Williamson Nanofluid Flow in the Rheology of Thermal Radiation, Joule Heating, and Chemical Reaction Using the Levenberg–Marquardt Neural Network Algorithm,*Frontiers in Energy Research,* 10 (2022), pp.1-23. https://doi.org/10.3389/fenrg.2022.965603.

[18] ShivaRao *et al.,*A Numerical Study on Unsteady MHD Williamson Nanofluid Flow Past a Permeable Moving Cylinder in the Presence of Thermal Radiation and Chemical Reaction, *Biointerface Research in Applied Chemistry*, 13 (2023), pp.1-19. https://doi.org/10.33263/briac135.436.

[19] Zegeye *et al.,* Combined Effects of Joule Heating and Binary Chemical Reaction of MHD Williamson Nanofluid on Darcy–Forchheimer Porous Medium Past Unsteady Stretching Cylinder, *International Journal of Thermofluids*, 20 (2023), pp.100474. https://doi.org/10.1016/j.ijft.2023.100474.

[20] Ijaz, Misbah *et al.,* Activation Energy and Dual Stratification Effects for Walter-B Fluid Flow in View of Cattaneo-Christov Double Diffusionon, *Heliyon* 5 (2019), pp.e01815. https://doi.org/10.1016/j.heliyon.2019.e01815.

[21] Salahuddin,T. *et al.,* Variable Thermo-Physical Characteristics of Carreau Fluid Flow by Means of Stretchable Paraboloid Surface with Activation Energy and Heat Generation, *Case Studies in Thermal Engineering* ,25 (2021) pp.100971. https://doi.org/10.1016/j.csite.2021.100971.

[22] C.Srinivas Reddy *et al.,*,Cattaneo–Christov Double Diffusion Theory for MHD Cross Nanofluid Flow towards a Vertical Stretching Sheet with Activation Energy,*International Journal of Ambient Energy* 43(1),(2021)pp.3924–33. https://doi.org/10.1080/01430750.2020.1852113.

[23] Saleem, Musharafa *et al.,* Impression of Nonlinear Radiation and Stefan Blowing on the Magneto Cross Nano-Williamson Fluid above Exponentially Stretching Sheet,*Results in Engineering* 17 (2023), pp.100864. https://doi.org/10.1016/j.rineng.2022.100864

[24] The MathWorks, Inc. (2018a). MATLAB R2018a [Computer software]. Natick, Massachusetts: The MathWorks, Inc.

Submitted: 28.03.2025.
Revised: 27.04.2025.
Accepted: 10.05.2025.